Supporting Information

Nanoscale Origin of Strong Charge Carrier Scattering at Grain Boundaries in Orthorhombic SnSe Semiconductor Thin Films

Xinyi He[1,2], *Kenji Matsuo*[1], *Takayoshi Katase*[1,3,*], *Kota Hanzawa*[3], *Hideto Yoshida*[4], *Shigenori Ueda*[5,6], *Hidenori Hiramatsu*[1,3], *Hideo Hosono*[1],*and Toshio Kamiya*[1,3,*]

[1] MDX Research Center for Element Strategy, Institute of Integrated Research, Institute of Science Tokyo, 4259 Nagatsuta, Midori, Yokohama 226-8501, Japan

[2] Kanagawa Institute of Industrial Science and Technology, 705-1 Shimoimaizumi, Ebina, Kanagawa 243-0435, Japan

[3] Materials and Structures Laboratory, Institute of Integrated Research, Institute of Science Tokyo, 4259 Nagatsuta, Midori, Yokohama, 226-8501, Japan

[4] SANKEN, Osaka University, 8-1 Mihogaoka, Ibaraki, Osaka 567-0047, Japan

[5] Research Center for Electronic and Optical Materials, National Institute for Materials Science (NIMS), 1-1 Namiki, Tsukuba, Ibaraki, 305-0044, Japan

[6]Synchrotron X-ray Station at SPring-8, NIMS, 1-1 Sayo, Hyogo 679-5148, Japan

* Correspondence to: katase.t.aa@m.titech.ac.jp, kamiya.t.aa@m.titech.ac.jp

Contents

Fig. S1. Growth rate dependence of electronic properties and crystallinity of SnSe films grown at 500 °C on glass substrates.

Fig. S2. X-ray diffraction (XRD) analysis of SnSe films grown at different temperatures on glass substrates.

Fig. S3. Atomic force microscopy (AFM) images of SnSe films grown at different temperatures on glass substrates.

Fig. S4. Cross-sectional scanning transmission electron microscope (STEM) image of SnSe film grown at 500 °C on glass substrate.

Fig. S5. Out-of-plane and in-plane XRD patterns of SnSe film grown at 500 °C on MgO substrate.

Fig. S6. AFM image of SnSe film grown at 500 °C on MgO substrate.

Fig. S7. Cross-sectional STEM image of SnSe film grown at 500 °C on MgO substrate.

Fig. S8. Lattice parameters and volumes of SnSe films.

Fig. S9. Atomic ratio of Sn and Se in SnSe films.

Fig. S10. Arrhenius plots of carrier concentration for SnSe films.

Fig. S11. Electronic structure analysis of SnSe films.

Fig. S12. Crystal structure analysis of SnSe models with 1 Sn or 1 Se vacancies.

Optimization of growth rate for SnSe films on glass substrates

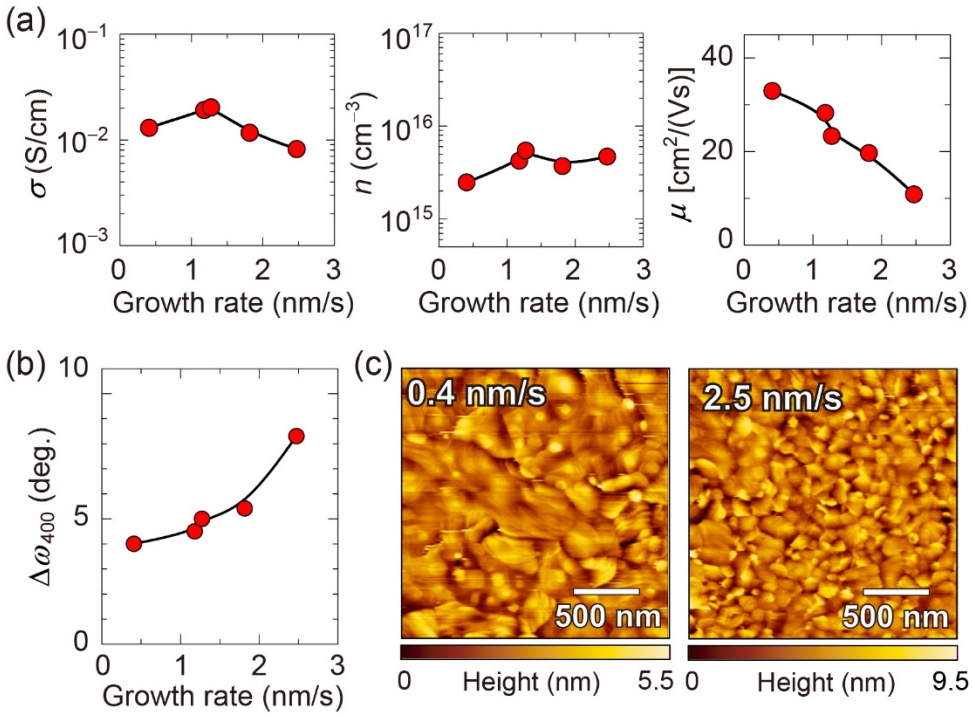

Figure S1. Growth rate dependence of room-temperature (RT) electronic properties and crystallinity of SnSe films deposited at 500 °C on glass substrates. (a) electronic conductivity (σ), carrier concentration (n), and carrier mobility (μ) vs. growth rate. (b) FWHM values ($\Delta\omega_{400}$) of rocking curves for 400 diffractions for SnSe phase vs. growth rate. (c) AFM images for SnSe films deposited under growth rate of 0.4 nm/s and 2.5 nm/s.

SnSe thin film growth on glass and MgO (001) substrates

Figure S2 summarizes XRD patterns of SnSe films deposited by changing the growth temperature (T_g) from RT to 500 °C on glass substrates. For out-of-plane XRD patterns (**Fig. S2(a)**), only *h*00 diffraction peaks of SnSe phase were observed even for the films at T_g = RT. The intensity of *h*00 diffraction peaks became stronger and the peak width became sharper with increase of T_g. The FWHM values of 400 diffraction peaks decreased from 10.5° to 4.8° with increase of T_g (**Fig. S2(b)**). For in-plane XRD patterns (**Fig. S2(c)**), the peak intensity of 111 diffraction was strongest for films with T_g = RT, but the intensity of 011, 002, 020, and 022 diffraction peaks increased largely with increase of T_g. From these results, the *a*-axis orientation was dominant for SnSe films deposited even at RT, but the degree of *a*-axis orientation increased by increasing T_g up to 500 °C. **Figure S3** summarizes AFM images of SnSe films grown on glass substrates. Small crystallites were observed for T_g = RT and 100 °C, while the grain size largely increased with increase of T_g up to 500 °C. **Figure S4** shows the STEM images of SnSe film deposited on glass substrate at T_g = 500 °C. The multi-domain structures with different contrast were observed in the cross-sectional STEM image (**Fig. S4(a)**), where the GBs were clearly observed as indicated by arrows. In the atomic-scale STEM image of SnSe film (**Fig. S4(b)**), the stacking structure of Sn-Se molecular layers were observed along out-of-plane direction.

Figure S5 shows the out-of-plane and in-plane XRD patterns of SnSe film grown at T_g = 500 °C on MgO (001) substrate.[1] The *h*00 diffraction peaks of SnSe and 00*l* diffraction peaks of MgO were observed for out-of-plane XRD pattern (**Fig. S5(a)**), and the 002 diffraction peak of SnSe and 200 diffraction peak of MgO were observed for in-plane XRD pattern (**Fig. S5(b)**). The FWHM value of 400 diffraction peak was 0.2° (inset of **Fig. S5(a)**). For in-plane ϕ scan of 002 diffraction of SnSe, diffraction peaks appeared at every 90° and exhibited 4-fold rotational symmetry. However, SnSe has orthorhombic lattice structure, and thus the SnSe was epitaxially grown on MgO substrate with 90° rotational domain structure. The epitaxial relationship was

[100] SnSe || [001] MgO for out-of-plane direction and [010][001]SnSe || MgO [100] for in-plane direction. From AFM image of the SnSe epitaxial film (**Fig. S6**), the spiral domain growth was observed, where the average domain size was ~100 nm. **Figure S7** shows the cross-sectional STEM image around the interface of SnSe film and MgO substrate. The clear layered atomic structure of SnSe phase was seen from the vicinity of the interface to bulk region, where the coherent interface between SnSe and MgO was formed, as indicated by vertical lines.

Figure S8 summarizes the lattice parameters and lattice volume of SnSe films. With increase of T_g, the *a*-axis lattice parameter (*a*) decreased and *c*-axis lattice parameter (*c*) increased respectively, while the *b*-axis lattice parameter (*b*) was almost constant (**Figs. S8(a-c)**). As the result, the lattice volume (*V*) increased and became close to that of SnSe bulk[2] at higher T_g. For SnSe epitaxial film on MgO substrate, the *c* was slightly smaller and *a* was larger than those of the film grown on glass substrate at same T_g = 500 °C. It is considered that the in-plane compressive strain along *c*-axis decreases *c*, while the expansion of *a* is caused by the epitaxial strain. **Figure S9** shows the T_g dependence of Sn and Se atomic ratio in the SnSe films, where the Se/Sn ratio was almost constant at 1.00–1.01, regardless of the T_g change.

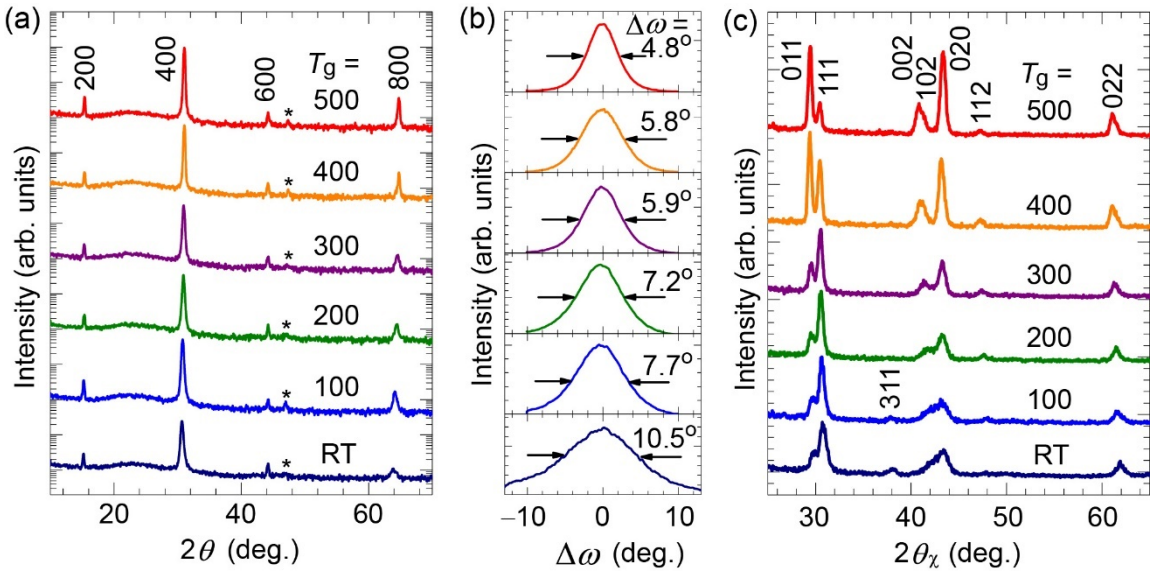

Figure S2. XRD analysis of SnSe films deposited at T_g from RT to 500 °C on glass substrates. (a) Out-of-plane XRD patterns. (b) Rocking curves of 400 diffraction peaks. (c) In-plane XRD patterns. The diffraction indices of SnSe phase are described near the corresponding diffraction peaks in (a,c). Weak peaks marked by asterisks correspond to reflections from sample stage.

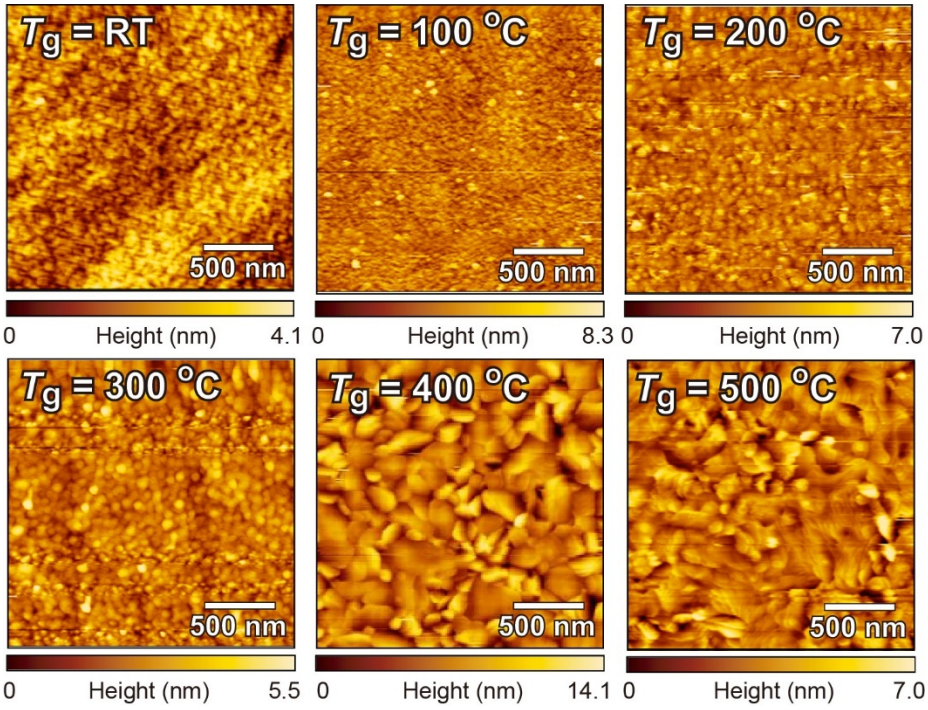

Figure S3. AFM images of SnSe films deposited on glass substrates at T_g = RT–500 °C.

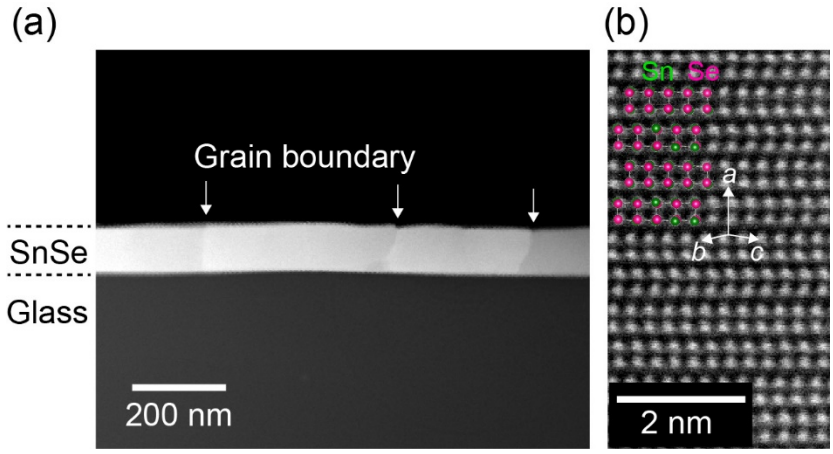

Figure S4. (a) Cross-sectional STEM image of SnSe film deposited on glass substrate at T_g = 500 °C. The arrows indicate the position of grain boundaries. (b) Atomic-scale STEM image of SnSe layer.

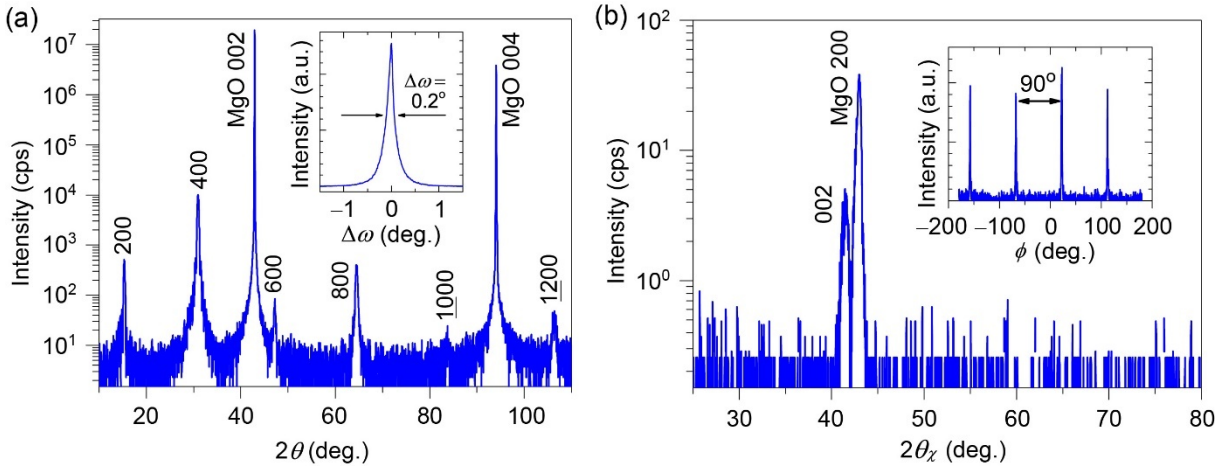

Figure S5. (a) Out-of-plane and (b) in-plane XRD patterns of SnSe film deposited on MgO (001) substrate at T_g = 500 °C.[1] Rocking curve of 400 diffraction for SnSe phase is shown in the inset of (a). In-plane ϕ scan of 002 diffraction for SnSe phase is shown in the inset of (b).

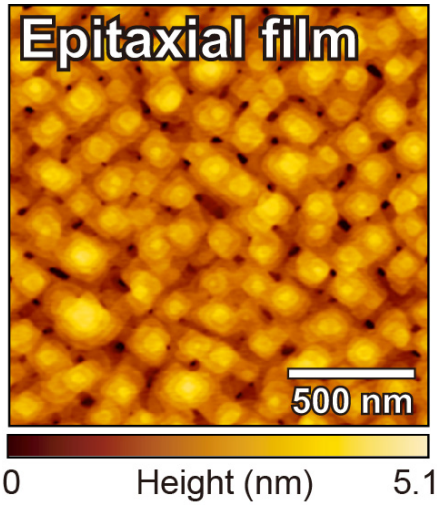

Figure S6. AFM image of SnSe epitaxial film deposited on MgO (001) substrate at T_g = 500 ^oC.[1]

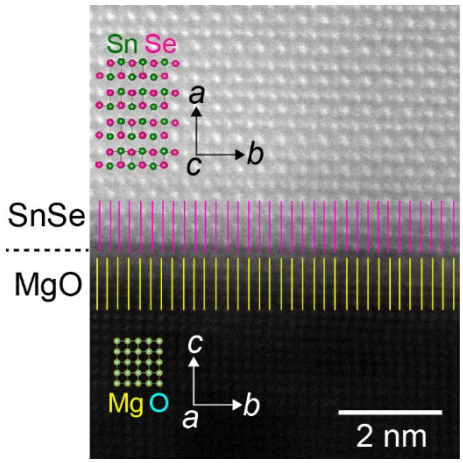

Figure S7. Cross-sectional STEM image of SnSe film deposited on MgO (001) substrate at T_g = 500 ^oC. The horizontal dotted line indicates the film/substrate interface position.

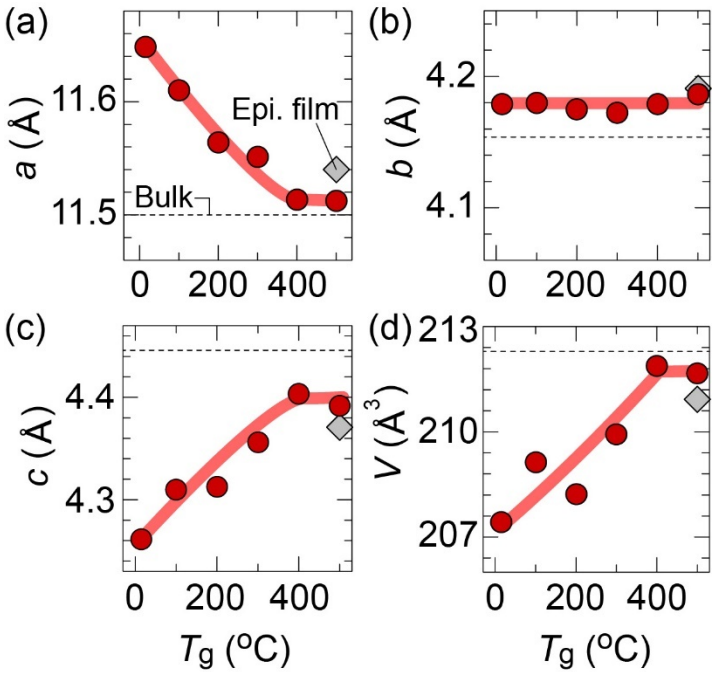

Figure S8. (a-c) Lattice parameters for (a) *a*-axis, (b) *b*-axis, (c) *c*-axis, and (d) lattice volume (*V*) as a function of T_g for SnSe films on glass substrates. Those of SnSe epitaxial film with T_g = 500 °C are also shown for comparison. The dotted lines indicate the *a*, *b*, *c* and *V* of SnSe bulk.[2]

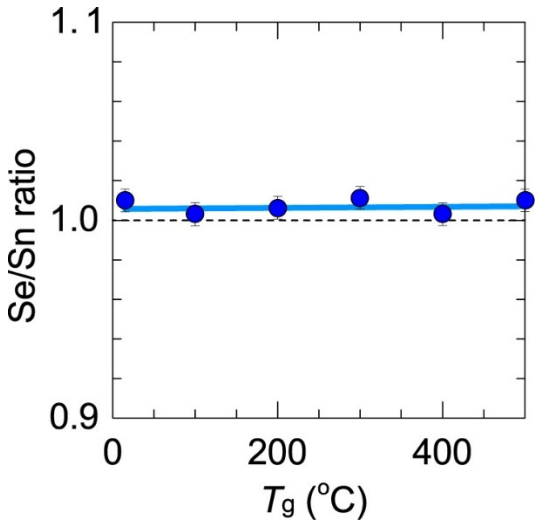

Figure S9. Atomic ratio of Sn and Se in SnSe films grown on glass substrates at different T_g = RT–500 °C. The plots indicate the average values from 15 measurements by electron probe micro-analyzer (EPMA) and the error bars indicate the standard deviation.

Carrier transport analysis

Arrhenius plots of n using $\ln\left(nT^{-\frac{3}{4}}\right) = \left(-\frac{E_a}{k_B}\right)\left(\frac{1}{T}\right) + \ln\left(\sqrt{\frac{n_V n_A}{T^{3/2}}}\right)$ for the free electron apporximation are shown in **Fig. S10(a)**, where E_a is the activation energy, n_v the effective density of states (DOS) of the valence band, and n_A the acceptor state density, respectively. The linear trend was observed in whole T range. The estimated E_a of n increased from 0.150 eV to 0.196 eV with increasing T_g from RT to 500 °C (**Fig. S10(b)**), indicating the shallower acceptor level in SnSe films grown at lower T_g. The high n_A ~2.1×10^{20} cm^{-3} was observed for SnSe film at T_g = RT, but it decreased to 7.1×10^{19} cm^{-3} with increasing T_g to 500 °C (**Fig. S10(c)**). On the other hand, the SnSe epitaxial film exhibited slightly lower E_a = 0.186 eV but lower n_A = 2.9×10^{19} cm^{-3}.

In order to know the electronic structure change of SnSe films with different T_g, the optical absorption and hard X-ray photoemission spectroscopy (HAXPES) measurements were performed for SnSe films grown at T_g = RT and 400 °C on glass substrates. Optical bandgap (E_g) was evaluated by measuring transmittance (T) and reflectance (R) spectra, where the optical absorption coefficient (α) was estimated by the relationship $\alpha = \log_e[(1-R)/T]/d$. The HAXPES measurement was performed at the BL15XU undulator beamline (the excitation x-ray energy: hv = 5953.4 eV) of SPring-8 at RT. The binding energy was calibrated with the Fermi level (E_F) of an evaporated Au thin film, and the total energy resolution was set to 240 meV. The estimated E_g were almost similar at 0.94–0.96 eV (**Fig. S11(a)**). Meanwhile, the energies of valence band maximum (E_{VBM}), determined by extrapolating the leading edge shown by the black dotted lines, were located at 0.14 eV from E_F for T_g = RT and 0.20 eV for T_g = 400 °C, indicating that the E_{VBM} shifted to a deeper energy by increasing the T_g (**Fig. S11(b)**). We constructed band alignment from the measured E_g and the E_{VBM} (**Fig. S11(c)**). E_F located near the VBM and the E_F position moved away from the VBM due to the decrease of n with increasing the T_g. The increase of n can be explained by the increase of Sn vacancy (V_{Sn}) in SnSe films with decreasing

T_g. We investigated the structure change by using the 1×3×3 supercell with 1 V_{Sn} or 1 Se vacancy (V_{Se}) in SnSe with 72 atoms. The relaxed crystal structure is shown in **Fig. S12(a)**. The V_{Sn} formation relaxed the strain in the Sn-Se molecular layers along the *c*-axis, resulting in the decrease of *c*, while *a* increase (**Fig. S12(b)**), which is consistent with the experimental results (**Fig. S8**). The small amount of naturally formed V_{Sn} in SnSe films would work as shallow acceptors for p-type conduction. Larger amount of V_{Sn} was formed at low T_g condition, but it was suppressed by increasing T_g, resulting in the decrease of *n*.

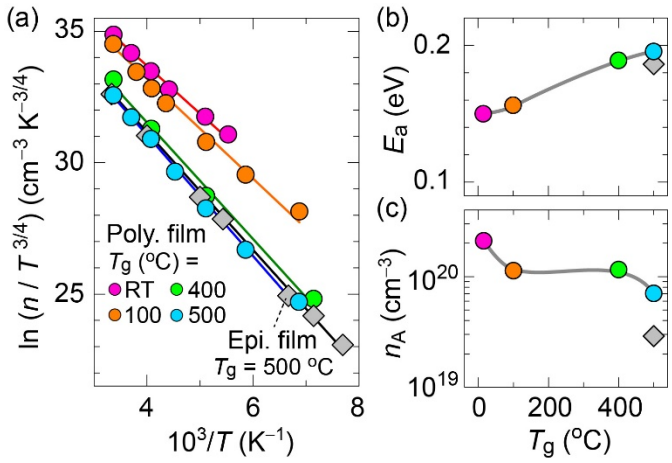

Figure S10. (a) Arrhenius plots of carrier concentration (*n*) for SnSe films. (b,c) T_g dependence of (b) activation energies (E_a) and (c) acceptor state density (n_A).

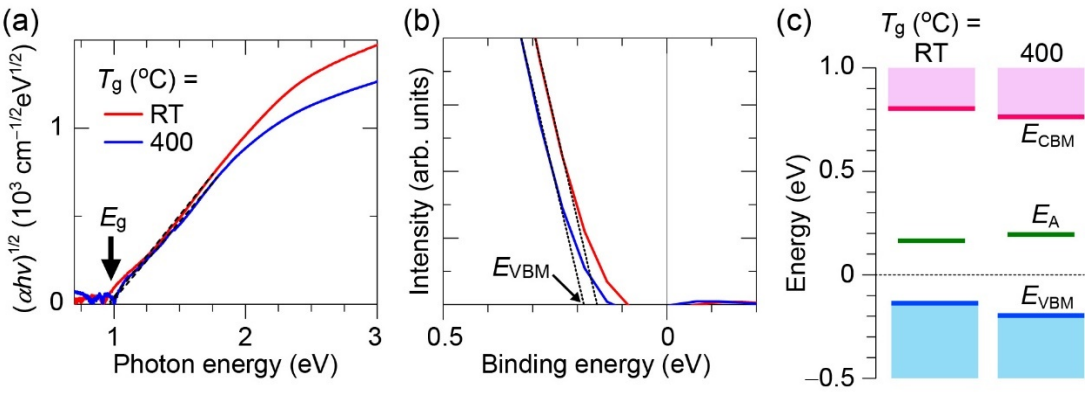

Figure S11. (a) $(\alpha h\nu)^{1/2}$ plots for SnSe films grown on glass substrates at T_g = RT and 400 °C to estimate the in-direct gaps (E_g). The arrow indicates the band gap position. (b) HAXPES

spectra near VBM. The energy of the VBM (E_{VBM}) is estimated by the leading-edge analysis, as indicated by dotted black lines. (c) Schematic electronic structure. The energy of conduction band minimum (E_{CBM}) and E_{VBM} are indicated by red and blue lines, respectively. The acceptor level (E_A), estimated from the Arrhenius plots of n (**Fig. S10(b)**), are also drawn by green lines.

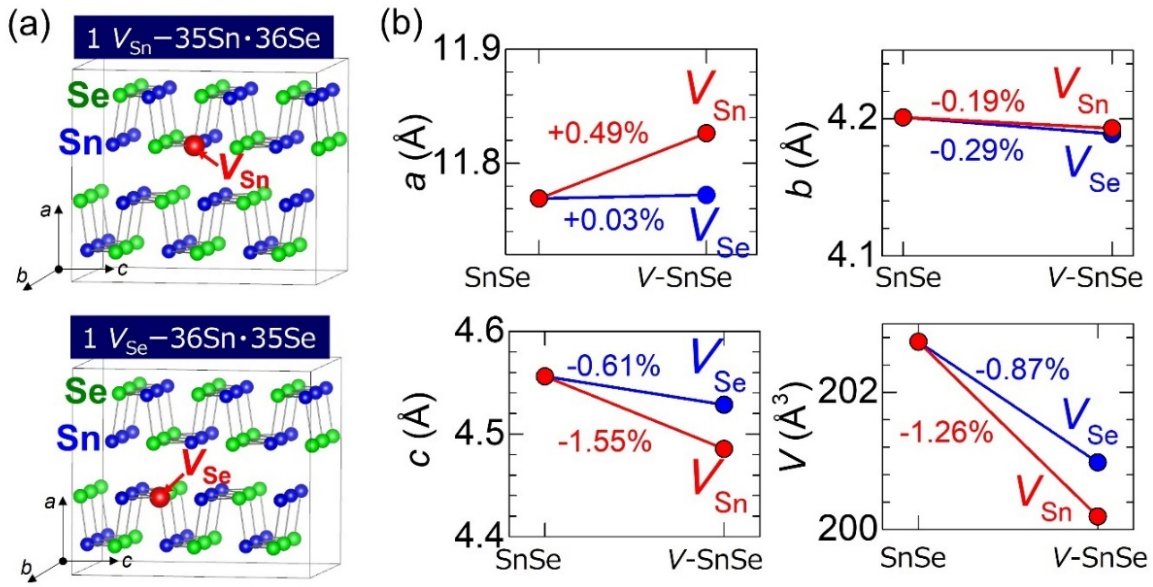

Figure S12. Relaxed structures of 72-atom supercell SnSe models with (a) 1 Sn vacancy (V_{Sn}) and (b) 1 Se vacancy (V_{Se}). The V_{Sn} or V_{Se} concentration is 2.8%. (b) Comparison of lattice parameters (a,b,c) and volumes (V) for perfect SnSe model excluding vacancies and SnSe models involving V_{Sn} and V_{Se}.

References

(1) He, X.; Chen, J.; Katase, T.; Minohara, M.; Ide, K.; Hiramatsu, H.; Kumigashira, H.; Hosono, H.; Kamiya, T. High-Mobility Metastable Rock-Salt Type (Sn,Ca)Se Thin Film Stabilized by Direct Epitaxial Growth on a YSZ (111) Single-Crystal Substrate. *ACS Appl. Mater. Interfaces* **2022**, *14*, 18682−18689.

(2) Wu, P.; Ishikawa, Y.; Hagihala, M.; Lee, S.; Peng, K.; Wang, G.; Torii, S.; Kamiyama, T. Crystal structure of high-performance thermoelectric materials by high resolution neutron powder diffraction. *Physica B: Condens. Mater.* **2018**, *551*, 64−68.